JOURNAL OF AIRCRAFT
Vol. 42, No. 2, March–April 2005

# Condensation on ONERA M6 and F-16 Wings in Atmospheric Flight: Numerical Modeling

Kevin A. Goodheart* and Günter H. Schnerr†
*Technical University of Munich, D-85748 Garching, Germany*

**A numerical investigation of the adiabatic and condensing flowfield around the ONERA M6 and F-16 Falcon wing is performed. For the ONERA M6 wing, three different mean aerodynamic chord $c_{\mathrm{mac}}$ lengths, 0.5, 1.0, and 2.0 m, three angles of attack, 1.07, 3.06, and 6.06 deg, and three different number densities of particles, $10^6$, $10^{12}$, and $10^{16}$ $\mathrm{m}^{-3}$, are analyzed. At $10^6$ $\mathrm{m}^{-3}$, the flow is dominated by homogeneous condensation, and due to the large chord length, the effects of condensation are small. As the particle density increases, a mixture of homogeneous/heterogeneous condensation occurs at $10^{12}$ $\mathrm{m}^{-3}$, and at $10^{16}$ $\mathrm{m}^{-3}$, only heterogeneous condensation occurs. For the F-16 Falcon wing, the size of the wing and the number density of particles $10^{12}$ $\mathrm{m}^{-3}$ are kept constant. The angle of attack and freestream Mach number are changed, where a decrease in the lift-to-drag ratio reached 20%. In general, if the wing is experiencing separation, condensation can improve the lift-to-drag ratio, whereas for attached flow with small flight angles, condensation reduces the lift-to-drag ratio.**

## Nomenclature

| | | |
|---|---|---|
| $a$ | = | speed of sound, m/s |
| $c$ | = | chord, m |
| $c_{D,p}$ | = | pressure drag coefficient |
| $c_f$ | = | integral friction coefficient |
| $c_L$ | = | lift coefficient |
| $c_p$ | = | pressure coefficient |
| $E$ | = | total internal energy, J/kg |
| $f_{\beta^*}$ | = | turbulent closure coefficient |
| $g$ | = | condensate mass fraction |
| $J$ | = | nucleation rate, $1/\mathrm{m}^3 \cdot \mathrm{s}$ |
| $k$ | = | turbulent kinetic energy, $\mathrm{m}^2/\mathrm{s}^2$ |
| $Kn$ | = | Knudsen number |
| $L$ | = | latent heat (heat of vaporization), J/kg |
| $M$ | = | Mach number |
| $N_{\mathrm{het},0}$ | = | number density of particles, $1/\mathrm{m}^3$ |
| $n_{\mathrm{hom}}$ | = | number density of droplets, 1/kg |
| $P$ | = | turbulent production, $\mathrm{N/m}^2 \cdot \mathrm{s}$ |
| $p$ | = | pressure, bar |
| $q$ | = | heat flux, $\mathrm{W/m}^2$ |
| $q_i$ | = | $-k(\mathrm{d}T/\mathrm{d}x_i)$ |
| $r$ | = | average droplet radius, m |
| $R_0$ | = | mixture gas constant, $\mathrm{J/kg} \cdot \mathrm{K}$ |
| $Re$ | = | Reynolds number |
| $R_p$ | = | particle radius, m |
| $T$ | = | temperature, K |
| $u, v, w$ | = | velocity components, m/s |
| $x, y, z$ | = | Cartesian coordinates, m |
| $y^+$ | = | dimensionless wall distance |
| $\alpha$ | = | angle of attack |
| $\beta, \beta^*$ | = | turbulent closure coefficients 0.83, 0.0895 |
| $\gamma$ | = | turbulent closure coefficient 0.575; heat capacity ratio |
| $\delta_{ij}$ | = | Kronecker delta |
| $\epsilon, \eta, \zeta$ | = | metrics |
| $\lambda$ | = | mean free path, m |
| $\mu_l$ | = | molecular viscosity, $\mathrm{kg/m} \cdot \mathrm{s}$ |
| $\rho$ | = | density, $\mathrm{kg/m}^3$ |
| $\tau$ | = | shear stress, $\mathrm{N/m}^2$ |
| $\phi$ | = | humidity, % |
| $\omega$ | = | specific dissipation rate, 1/s |

*Subscripts*

| | | |
|---|---|---|
| $d$ | = | droplet |
| $g$ | = | gas |
| het | = | heterogeneous |
| hom | = | homogeneous |
| $l$ | = | liquid |
| $N$ | = | normal |
| mac | = | mean aerodynamic chord |
| $v$ | = | vapor |
| 01 | = | reservoir, stagnation |
| $\infty$ | = | freestream |
| $*$ | = | critical state |

Received 4 November 2003; revision received 7 February 2004; accepted for publication 10 February 2004. 

*Doctoral Candidate, Lehrstuhl für Fluidmechanik–Fachgebiet Gasdynamik, Boltzmannstraße 15.

†Professor, Lehrstuhl für Fluidmechanik–Fachgebiet Gasdynamik, Boltzmannstraße 15.

## Introduction

In transonic flow, the combination of large expansion rates and moist air compared to dry air can give remarkable alternations in the lift and drag coefficients. The high latent heat of water with the addition of a large acceleration (expansion/drop in temperature) around a body can produce a supersaturated flowfield and, thus, the onset of homogeneous condensation. With the addition of foreign nuclei in the flowfield, it is also possible to achieve condensation even if the expansion is not as large. The classical test case of the ONERA M6 wing is used to examine the effects of condensation because of the available geometry and adiabatic pressure data.[1] Schnerr and Dohrmann[2] have done extensive two-dimensional Euler simulations for airfoils under atmospheric flight and wind-tunnel conditions. This distinction is made because of the dependence of length scale for condensation to occur. Yamamoto et al.[3] also calculated the flowfield around the ONERA M6 wing for a mean chord length of 0.646 m under different relative humidities but only for homogeneous condensation. Recently, Yamamoto[4] calculated the delta wing for homogeneous and heterogeneous condensation for different length scales and operating conditions. This paper will only deal with atmospheric flight parameters using a $c_{\mathrm{mac}}$ of 0.5, 1, and 2 m. There are many factors (grid, turbulence model, angle of attack, length scale, etc.) that affect the condensing flowfield around a three-dimensional body. It is the aim of this paper to determine their impact and understand the reasons behind their influence. The first step will be to examine the number density of particles, $N_{\mathrm{het},0}$; three values are used that produce dominating homogeneous

condensation ($10^6$ m$^{-3}$), heterogeneous condensation ($10^{16}$ m$^{-3}$), and a mixture of the two ($10^{12}$ m$^{-3}$). A typical value for particle density is $\sim 10^{12}$ m$^{-3}$. Yamamoto[4] also used this value for a 76-deg sharp-edged single-delta wing. With these values of $N_{\text{het},0}$, the different $c_{\text{mac}}$ will be calculated with three different angles of attack, 1.07, 3.06, and 6.06 deg. The ONERA M6 wing is a well-established test case, but it is also of interest to determine the effects of the lift-to-drag ratio on a different wing configuration, for example, a supercritical wing designed for high-speed flight. The F-16 Falcon wing is chosen mainly because the root and tip airfoil sections are known; then a linear approximation of the wing can be made from the two airfoil sections (zero twist).

## Numerical Method

The Reynolds averaged Navier–Stokes compressible equations are discretized using a three-dimensional node-centered finite volume method based on the work of Benetschik.[5] The code is written from a (Habilitation) report that was developed for turbomachinery simulations. The report details how to determine the metrics, convective and diffusive fluxes, boundary conditions, etc. Thus, the Benetschik report was used as a starting point for our code, where additions/alternations were added to accommodate our research. Examples of additions include $k$–$\omega$ based turbulence models compared to $k$–$\epsilon$, condensation transport equations, boundary conditions for external flow, and the AUSMD scheme instead of the Roe scheme for the convective fluxes. Two additional turbulent equations and three additional transport equations for the liquid phase are introduced to complete the modeling. The vector form of the 10-equation set is a follows:

$$\frac{\partial \boldsymbol{U}}{\partial t} + \frac{\partial \boldsymbol{E}_i}{\partial x_i} = \boldsymbol{S} \tag{1}$$

where the vectors are given by

$$\boldsymbol{U} = \begin{vmatrix} \rho \\ \rho u \\ \rho v \\ \rho w \\ \rho e \\ \rho k \\ \rho \omega \\ \rho g_{\text{hom}} \\ \rho n_{\text{hom}} \\ \rho g_{\text{het}} \end{vmatrix}, \qquad \boldsymbol{E} = \begin{vmatrix} \rho u_i \\ \rho u_1 u_i + \delta_{i1} p - \tau_{i1} \\ \rho u_2 u_i + \delta_{i2} p - \tau_{i2} \\ \rho u_3 u_i + \delta_{i3} p - \tau_{i3} \\ (\rho E_i + p) u_i - u_1 \tau_{i1} - u_2 \tau_{i2} - u_3 \tau_{i3} + q_i \\ \rho k u_i \\ \rho \omega u_i \\ \rho g_{\text{hom}} u_i \\ \rho n_{\text{hom}} u_i \\ \rho g_{\text{het}} u_i \end{vmatrix}$$

$$\boldsymbol{S} = \begin{vmatrix} 0 \\ 0 \\ 0 \\ 0 \\ 0 \\ P - \rho f_{\beta^*} k\omega \\ \gamma \dfrac{k}{\omega} P - \beta \omega^2 \\ \dfrac{4}{3}\pi \varrho l \left( r_{\text{hom}}^{*3} J_{\text{hom}} + 3\varrho n_{\text{hom}} \bar{r}_{\text{hom}}^2 \dfrac{\mathrm{d}r_{\text{hom}}}{\mathrm{d}t} \right) \\ J_{\text{hom}} \\ 4\pi \rho_l \left( n_{\text{het}} \bar{r}_{\text{het}}^2 \dfrac{\mathrm{d}r_{\text{het}}}{\mathrm{d}t} \right) \end{vmatrix}$$

$$E = \frac{\gamma}{\gamma - 1}\left(\frac{p}{\rho} - \frac{2}{3}k\right) + k - gL - \frac{p}{\rho} + \frac{1}{2}(u^2 + v^2 + w^2)$$

$$p = \rho T (R_0 - g R_v) + \frac{2}{3}\rho k$$

where $q$ and $\tau$ are the standard heat flux and shear stress terms. The two source terms for the turbulence model are based on the explicit algebraic stress model (EASM) ($k$–$\omega$) (Ref. 6). The three remaining source terms are for the liquid phase. The equation for $g_{\text{hom}}$ has two components in the source term $\boldsymbol{S}(\mathbf{8})$, which represent the radius of a critical cluster, and once a critical cluster is formed, the term on the right controls growth/evaporation.

Droplet growth is related by an important parameter called the Knudsen number $Kn = 7\lambda/2r_d$. It is the ratio of the mean free path of the molecules to the diameter of the droplet. Very large values of Knudsen number relate to the inner Knudsen layer, where transfer is controlled by kinetics and intermolecular collisions are unimportant.[7] Very small Knudsen numbers relate to the continuum regime, where growth is controlled by diffusion. A contradiction exist in the literature on how one determines the free mean path,

$$\lambda = 2\mu\sqrt{RT}\Big/p \tag{2}$$

Wegener and Mack[8] maintain collisions between gas molecules are not important; thus, the pressure in Eq. (2) is based on the partial pressure of the vapor. However, Young[7] and Peeters et al.[9] maintain it is the mixture pressure that must be used in the calculation of the mean free path. The difference between for the two pressures is very large, for example, at 295 K, 1 bar, $M_\infty = 0.8$, and 90% humidity, $\lambda_{g-v} = 0.086$ $\mu$m and $\lambda_{v-v} = 3.6$ $\mu$m. In this paper, the droplet growth model is based on the Hertz–Knudsen law, which is valid for a vapor/carrier gas mixture because 1) the droplet size remains smaller than the mean free path and 2) the high mass fraction of inert carrier gas keeps the temperature gradients to a minimum in the environment. When the Wegener and Mack definition[8] for mean free path is used, $Kn \gg 1$ for all simulations, but if the Young[7] and Peeters et al.[9] definition is applied, $Kn \gtrsim 1$. In this case, $Kn \gtrsim 1$, the Hertz–Knudsen law would be overpredicting the droplet growth.

The source term $\boldsymbol{S}(\mathbf{9})$ for the $n_{\text{hom}}$ equation is simply the nucleation rate. The nucleation rate of the condensate is modeled by the classical nucleation theory of Volmer, Frenkel, and Zel'dovich. With the $g_{\text{het}}$ equation, there is no $J_{\text{het}}$ term, and the droplet growth law is a source or sink term $\boldsymbol{S}(\mathbf{10})$, which also uses the Hertz–Knudsen law. It is valid in this case because the particle diameter is still smaller than the free mean path of the vapor–vapor or gas–vapor collisions. The relationship between $N_{\text{het},0}$ and $n_{\text{het}}$ is

$$n_{\text{het}} = N_{\text{het},0}(\rho/\rho_{01})$$

If the thermodynamic state is saturated, the critical droplet size is determined from

$$r_{\text{hom}}^* = \frac{2\sigma_\infty}{\rho_l R_v T \ln(p_v/p_s)}, \qquad \text{if} \quad (p_v > p_s) \tag{3}$$

$$r_{\text{hom}}^* = 0, \qquad \text{if} \quad (p_v < p_s) \tag{4}$$

If $n_{\text{hom}} > 0$, the homogeneous droplet radius is

$$\bar{r}_{\text{hom}} = \left(g_{\text{hom}}\Big/\tfrac{4}{3}\pi\rho_l n_{\text{hom}}\right)^{\frac{1}{3}} \tag{5}$$

The heterogeneous droplet radius is

$$\bar{r}_{\text{het}} = \left(\frac{\rho g_{\text{het}}}{\frac{4}{3}\pi\rho_l n_{\text{het}}} + r_p^3\right)^{\frac{1}{3}} \tag{6}$$

Two additional assumptions are made for the condensation modeling, where the liquid portion of the condensate is much smaller than the vapor/carrier gas mixture; thus, the condensate follows the path of the fluid flow (no momentum exchange or drag). The second big assumption is that there is no temperature difference between water droplet and vapor/gas carrier mixture.

The convective fluxes are solved using the AUSMD technique of Wada and Liou.[10] The diffusive terms are calculated based on a second-order central difference scheme (Benetschik[5]). The convective terms are third-order accurate in space using a total variation

diminishing MUSCL approach with Van Albada limiter to determine the left and right states. The time step is first-order explicit using local time stepping. The air and vapor are assumed a perfect gas.

## Boundary Conditions

The boundary conditions for the freestream require the total temperature $T_{01}$, pressure $p_{01}$, and angle of attack $\alpha$. A system of five equations are solved to obtain the velocity components, freestream pressure, and density. The five equations at the boundary are the normal momentum equation (7), constant entropy [Eq. (8)], constant total energy [Eq. (9)], $v = u\tan(\alpha)$, and $w = 0$. The denoted with an asterisk variables represent the primitive variables that were just solved at the recent time step, and the primitive variables on the right-hand side represent the corrected variables. (It is important to note that the fluxes on the boundary are solved as periodic, and then after a step in time is made, the specified boundary conditions are used to correct the primitive variables.) Solving the system of five equations compared to specifying one freestream condition allows the inlet to be closer to the wing, for example, a 10:1 chord ratio between inlet boundary and the wing,

$$u_N^* - 2\frac{a^*}{\gamma - 1} = u_N - 2\frac{a^*}{\gamma - 1} \tag{7}$$

$$\frac{p_{01}}{\rho_{01}^{\gamma}} = \frac{p}{\rho^{\gamma}} \tag{8}$$

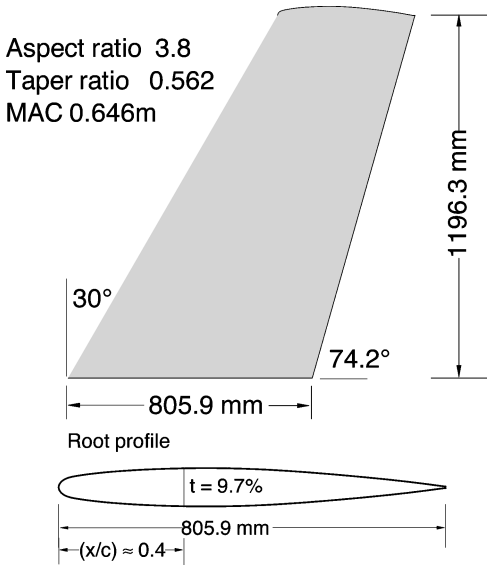


**Fig. 1 Geometry of the ONERA M6 wing based on experiment.**

$$\frac{\gamma}{\gamma - 1}\frac{p_{01}}{\rho_{01}} = \frac{\gamma}{\gamma - 1}\frac{p}{\rho} + \frac{1}{2}(u^2 + v^2 + w^2)$$

$$u_N = \frac{u\eta_x + v\eta_y}{\sqrt{\eta_x^2 + \eta_y^2}} \tag{9}$$

On the outlet, the average pressure across the boundary is set to the freestream pressure, which is calculated from the given Mach number and total pressure. This boundary condition allows the wake to pass through the boundary. The wing is a no-slip wall with the velocity and $k$ defined as zero. As long as $y^+$ is less than 2.5, $\omega$ is defined by

$$\omega = 0.0895\left(100\mu_l \Big/ \rho\Delta y_2^2\right) \tag{10}$$

where $(\Delta y_2)$ is the distance to the first grid point above the surface. The constant $\beta^* = 0.0895$ is needed because the EASM ($k$–$\omega$) model absorbs $\beta^*$ into $\omega$. Without $\beta^*$, Eq. (10) is one of the standard boundary condition for the $k$–$\omega$ model, which can be found by Wilcox.[11]

## Geometry

The ONERA M6[1] is a swept back wing with zero twist and no body fillets or strakes. The airfoil is symmetric with a 9.7% thickness at the root. Figure 1 shows the top view of the wing and root profile. The F16 Falcon consist of a NACA64A204 airfoil at the root and tip. The airfoil has a thickness of 4% with a sharp leading-edge. The wing has a leading-edge sweep angle of 40 deg with a straight trailing edge. Figure 2 shows the wing planform geometry and airfoil shape at the root and tip. Fortunately, data were found for the geometry of the F-16 wing for the airfoil shape, wingspan, and leading-edge sweep. The root and tip chord lengths were derived from a drawing of the top view of the plane.[12] A very important point must be clarified for both wings at the root profile. A wing–body junction is not modeled; for the time being, an Euler wall is assumed at the root profile.

## ONERA M6 Wing Results

### Adiabatic Verification

For all of the calculations low-level flight is assumed with $T_\infty = 293.15$ K, $p_\infty = 1$ bar, and $M_\infty \simeq 0.84$. Before beginning with the condensation results, a comparison is made between adiabatic experimental data and two different grids. The two grids are $213i \times 35j \times 25k$ and $213i \times 70j \times 47k$. The $i$ component was not doubled only the $j$ and $k$ were because these components were very coarse. Figure 3 shows a comparison of two different $c_p$ plots at 44 and 80% of the span. There are small differences in the $c_p$ results but not enough to warrant the extra computational time.

It is known that condensation requires denser grids compared to adiabatic calculations; thus, for one set of operating conditions

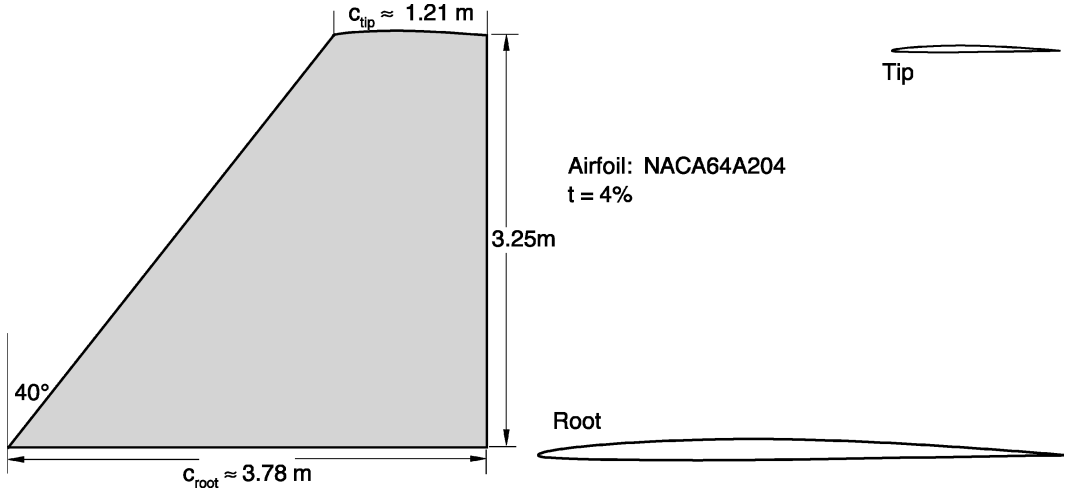


**Fig. 2 Geometry of F16 wing.**

**Table 1 Grid comparison using the drag, lift, and friction coefficient for different condensing flows**

| Grid | $N_{\text{het},0}$ [m$^{-3}$] | $c_{D,p}$ | $c_L$ | $c_f$ |
|---|---|---|---|---|
| A[a] | 0 | 0.0656 | 0.290 | 0.00336 |
| B[b] | 0 | 0.0608 | 0.292 | 0.00321 |
| A | $1 \times 10^6$ | 0.0663 | 0.287 | 0.00328 |
| B | $1 \times 10^6$ | 0.0612 | 0.291 | 0.00315 |
| A | $1 \times 10^{12}$ | 0.0683 | 0.310 | 0.00327 |
| B | $1 \times 10^{12}$ | 0.0637 | 0.312 | 0.00320 |
| A | $1 \times 10^{16}$ | 0.0714 | 0.338 | 0.00326 |
| B | $1 \times 10^{16}$ | 0.0664 | 0.337 | 0.00312 |

[a]Grid A $= 213i \times 35j \times 25k$. [b]Grid B $= 213i \times 70j \times 47k$.

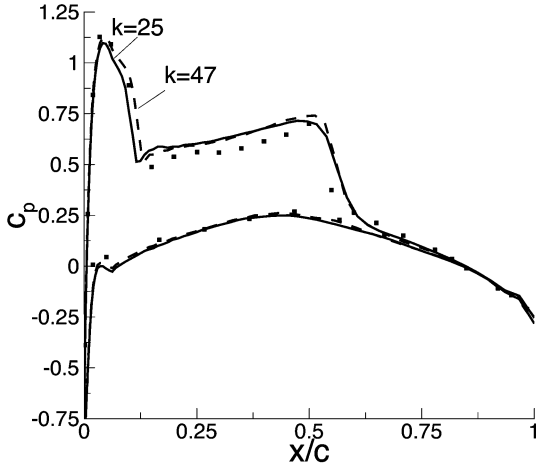


**a) 44% span**

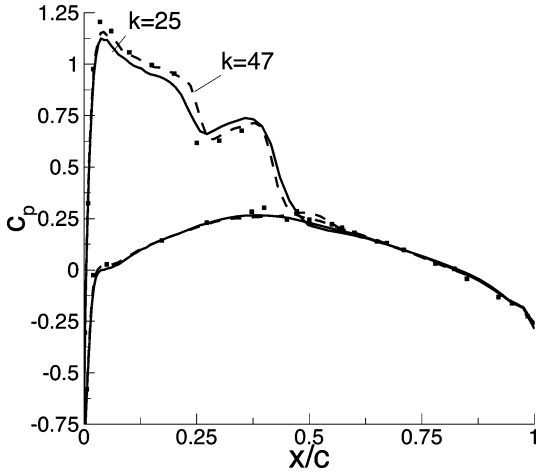


**b) 80% span**

**Fig. 3 ONERA M6 wing pressure coefficient between densities A = $213i \times 35j \times 25k$ and B = $213i \times 70j \times 47k$ compared and with experiment[1]; $M_\infty = 0.84$, $Re_{c_{\text{mac},\infty}} = 18.92 \times 10^6$, $c_{\text{mac}} = 1$ m, $\alpha = 3.06$ deg, and $\bar{y}^+ = 0.9$.**

condensation was also calculated for both grids. Table 1 is a comparison of the drag and lift coefficient for different particle densities between the two grids for $Re_{c_{\text{mac},\infty}} = 18.92 \times 10^6$, $c_{\text{mac}} = 1$ m, and $\alpha = 3.06$ deg. The main difference lies in the drag coefficient with a maximum difference around 7%, whereas the lift coefficients are nearly the same. Also both grids show the same trend; for example, at the maximum difference of 7% $N_{\text{het},0} = 1 \times 10^{16}$ m$^{-3}$, the relative change between the condensing and adiabatic case is 8.8% for grid A and 9.2% for grid B. Thus, the relative change is consistent. Even though there are slight differences, the remaining results will be based on the $213i \times 35j \times 25k$ grid.

Because the angle of attack is also changed, a comparison is made with experiment using grid A for $\alpha = 1.07$ and 6.06 deg

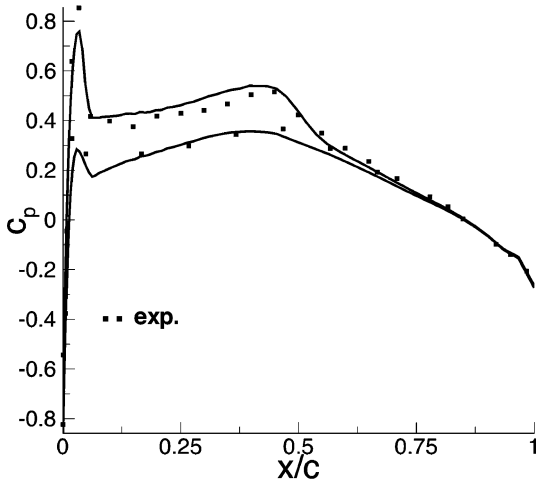


**a) 44% span**

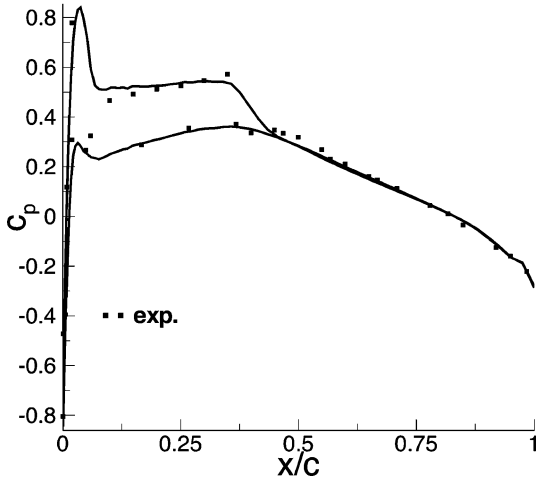


**b) 80% span**

**Fig. 4 ONERA M6 adiabatic pressure coefficient for an angle of attack of 1.07 deg compared with experiment[1]; $M_\infty = 0.84$, $Re_{c_{\text{mac},\infty}} = 18.96 \times 10^6$, $c_{\text{mac}} = 1$ m, and $\bar{y}^+ < 1.0$.**

(Figs. 4 and 5). The lower angle of attack has a weaker second shock, and the model is able to capture the position and strength, whereas for the larger angle of attack the double shock system is present near the root chord. However, moving to the tip, there is a separation zone that can be seen by the pressure coefficient at 80% span (Fig. 5b). The separation point is accurately predicted, but the recovery pressure is too high and then too low as it reaches the trailing edge.

### Range of Particle Density

For all of the following test cases the humidity is set equal to $\phi_0 \approx 16\%$, which corresponds to a freestream humidity of $\phi_\infty = 90\%$. This was chosen to get the maximum effect from condensation. One could lower the freestream humidity to 60 or 70% and then increase the freestream Mach number to 0.9 instead of 0.84 to see similar effects, but the lower Mach number was chosen to stay within the framework of the adiabatic experiments. The decrease in humidity with an increase in Mach number lowers $\phi_0$, but because the supersonic region is enlarged, there is a chance for a larger supersaturation or for the growth of heterogeneous condensation to occur. The particle radius is set to $R_p = 0.01$ $\mu$m. This value is chosen because the particle diameter is less than the mean free path of the vapor/carrier gas mixture, $K_n > 1 (\lambda_{g-v} = 0.086$ $\mu$m), and if a lower value was chosen (0.001 $\mu$m), heterogeneous effects would likely be small.

The first set of results compares the effect of changing the particle density while keeping the mean aerodynamic chord constant at 1.0 m

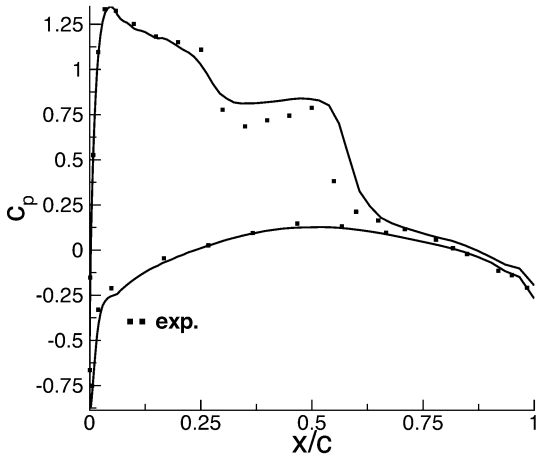


a) 44% span

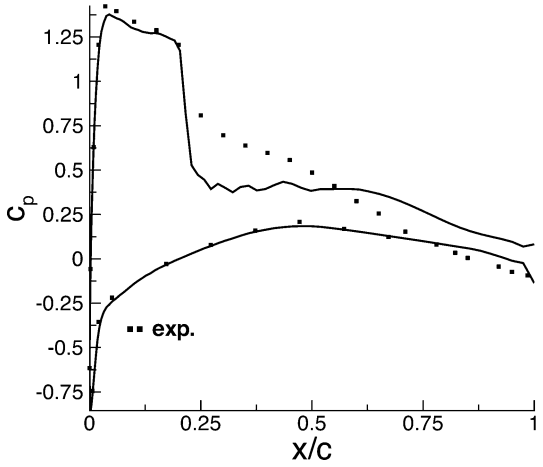


b) 80% span

**Fig. 5 ONERA M6 wing adiabatic pressure coefficient for an angle of attack of 6.06 deg compared with experiment[1]; $M_\infty = 0.84$, $Re_{c_{mac,\infty}} = 18.79 \times 10^6$, $c_{mac} = 1$ m, $\alpha = 6.06$ deg, and $\bar{y}^+ < 1.0$.**

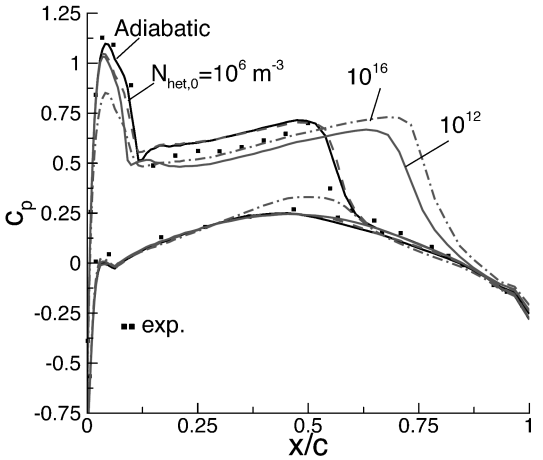


a) 44% span

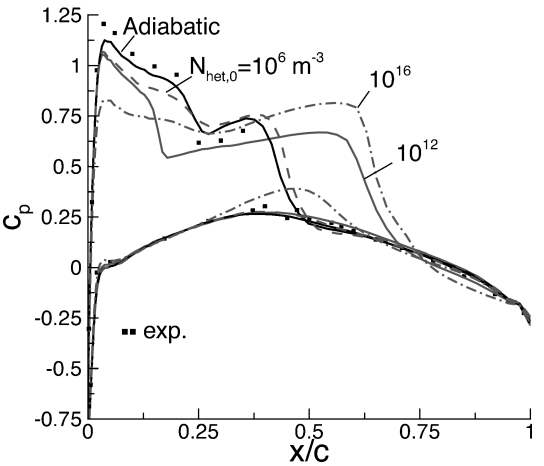


b) 80% span

**Fig. 6 ONERA M6 wing pressure coefficient for different particle densities; $M_\infty = 0.84$, $Re_{c_{mac,\infty}} = 18.92 \times 10^6$, $c_{mac} = 1$ m, $\alpha = 3.06$ deg, $R_p = 1 \times 10^{-8}$ m, and $\bar{y}^+ < 1$.**

and the angle of attack at 3.06 deg. In addition to the grid comparison, Table 1 also shows that the lift and drag coefficient increases with particle density. By examining $c_p$ plots, one can see where this increase comes from. Figure 6 compares the change in $c_p$ due to different particle densities at 44 and 80% span.

At a particle density of $10^6$ m$^{-3}$ (dashed line, Fig. 6) there is a small decrease in $c_p$ at the leading edge, but the position of the second shock is unchanged. The reason for this is that the flow is dominated by homogeneous condensation and the large acceleration at the leading edge causes a small amount of homogeneous condensation.

A particle density of $10^{12}$ m$^{-3}$ is a combination of homogeneous/heterogeneous condensation, where the homogenous condensate dominates at the leading edge and heterogeneous condensate dominates before the second shock on the suction side. The heterogeneous condensation pushes the second shock closer to the trailing edge and, thus, increases lift by delaying the increase in pressure due to the shock. Note that the pressure is higher before the second shock (Fig. 6), which decreases lift, but because the supersonic region is increased, the overall change is an increase in lift. The drag is increased because of the condensation occurring at the leading edge, which increases the static pressure; also the increased supersonic region after the maximum thickness of the airfoil on the suction side increases drag.

A particle density of $10^{16}$ m$^{-3}$ is dominated by heterogeneous condensation at the leading edge, before the second shock, and a small amount is forming on the pressure side. Here the supersonic region is extended more than the $10^{12}$ m$^{-3}$ case. The small bump on the pressure side has two negative effects; it increases drag and decreases lift. The drag is increased because of subsonic heat addition, whereas the pressure decrease occurs mostly after the maximum thickness. The maximum thickness is around $x/c = 0.4$. Drag is also greatly increased on the leading edge by the heat addition.

Figures 7 and 8 show the condensate mass fraction for $g_{hom}$ or $g_{het}$ and the adiabatic/condensing Mach 1 line at 44% chord. Figures 7 and 8 give an indication of how much condensation is occurring and what type. There is no figure for $g_{het}$ at $10^6$ and $g_{hom}$ at $10^{16}$ m$^{-3}$ because this type of condensation did not occur. The key elements of Figs. 7 and 8 is the increase in the sonic region with particle density and the different types of condensation. For all conditions, no condensation occurs in the boundary layer. The wavy structure at low values of $g_{het}$ is purely numerical due to the coarsening of the grid away from the profile.

### Mean Aerodynamic Chord Influence

At $10^6$-m$^{-3}$ particle density the effect of homogeneous condensation is very small for different $c_{mac}$. The maximum value of $\log_{10} J_{hom}$ at 44% span for a $c_{mac}$ of 0.5, 1.0, 2.0, and 4.0 m is 22.4, 20.6, 19.8, and 18.5 m$^{-3}$s$^{-1}$. A $c_{mac}$ of 0.5 is not a realistic wing size, but it is used to see how trends are developing and perhaps there are some components of a plane with this size. The smallest $c_{mac}$ of course, has the largest $J_{hom}$ because the smaller length scale has the largest cooling rate, but with this difference there is no noticeable difference in $c_p$ for $10^6$-m$^{-3}$ particle density.

For $10^{12}$-m$^{-3}$ particle density, there are large differences in $c_p$ for the range of $c_{mac}$, which translates to differences in drag and lift.

**Table 2 Summary of $c_{\text{mac}}$ comparison on condensation using the drag, lift, and friction coefficient; $N_{\text{het},0} = 1 \times 10^{12}$ m$^{-3}$**

| $c_{\text{mac}}$ | $Re_{c_{\text{mac}},\infty} \times 10^6$ | $c_{D,p}$ | $c_L$ | $c_f$ |
|---|---|---|---|---|
| 0.5 | 9.46 | 0.0668 | 0.294 | 0.00361 |
| 1.0 | 18.92 | 0.0683 | 0.310 | 0.00327 |
| 2.0 | 37.84 | 0.0697 | 0.326 | 0.00305 |
| 4.0 | 75.68 | 0.0705 | 0.323 | 0.00278 |

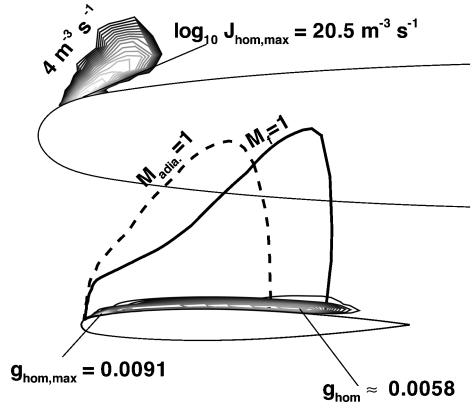


**a) Homogeneous**

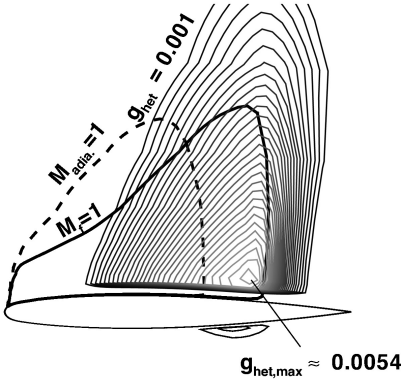


**b) Heterogeneous**

**Fig. 7 Condensate mass fraction and Mach 1 line at 44% span; $M_\infty = 0.84$, $Re_{c_{\text{mac}},\infty} = 18.92 \times 10^6$, $c_{\text{mac}} = 1$ m, $\alpha = 3.06$ deg, $N_{\text{het},0} = 1 \times 10^{12}$ m$^{-3}$, and $R_p = 1 \times 10^{-8}$ m.**

Table 2 is a summary of the change in the drag, lift, and friction coefficient for different $c_{\text{mac}}$. The drag and lift are both increasing with an increase in $c_{\text{mac}}$. The $c_f$ coefficient decreases, which corresponds to the increase in Reynolds number.

Figure 9 demonstrates the trend of increasing lift and drag found in Table 2, but the difference in lift between 2 and 4 m begins to plateau. In the $c_p$ plots, 4 m was not graphed because it follows the same trend as 2 m, and thus, it avoids a crowded graph. At a $c_{\text{mac}}$ of 2.0 or 4.0 m, the supersonic region is the largest and the leading edge is experiencing the greatest static pressure increase, which increases the drag. In Fig. 9, the difference in $\bar{y}^+$ for the different $c_{\text{mac}}$ ave$\bar{y}^+ = 0.5$, $c_{\text{mac}} = 0.5$; $\bar{y}^+ = 0.9$, $c_{\text{mac}} = 1.0$; and $\bar{y}^+ = 1.6$, $c_{\text{mac}} = 2.0$. This indicates that the grid was rescaled, and thus the distance of the first grid point also increases, but the values are still below 2.5.

### Angle of Attack

An interesting result with the higher angle of attack (6.06 deg) is that the drag is relatively constant except for the $10^{12}$-m$^{-3}$ case, with again the same trend for lift increasing as $N_{\text{het},0}$ increases. The drag for the higher angle of attack is partially dominated by the separation occurring near the tip. Figure 10a shows the pressure

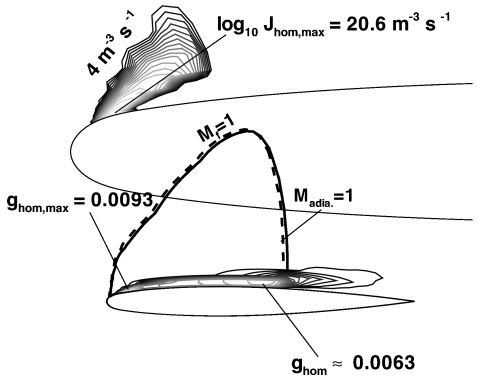


**a) Homogeneous**

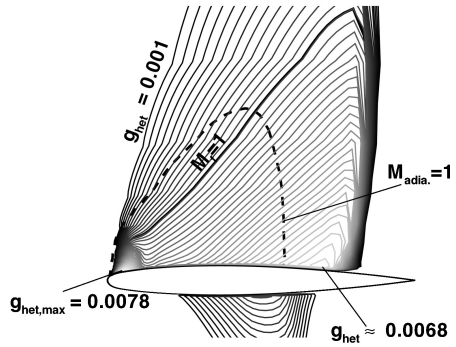


**b) Heterogeneous**

**Fig. 8 Condensate mass fraction and Mach 1 line at 44% span; $M_\infty = 0.84$, $Re_{c_{\text{mac}},\infty} = 18.92 \times 10^6$, $c_{\text{mac}} = 1$ m, $N_{\text{het},0} = 1 \times 10^6$ m$^{-3}$, $\alpha = 3.06$ deg, and $R_p = 1 \times 10^{-8}$ m.**

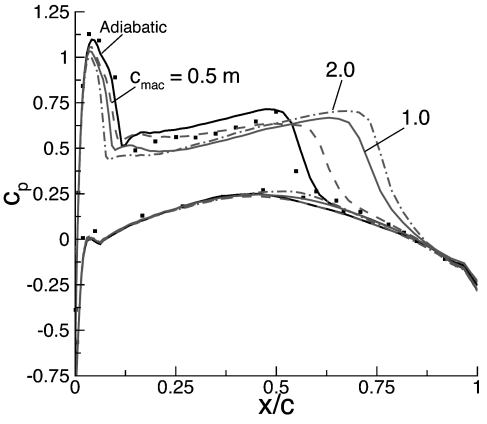


**a) 44% span**

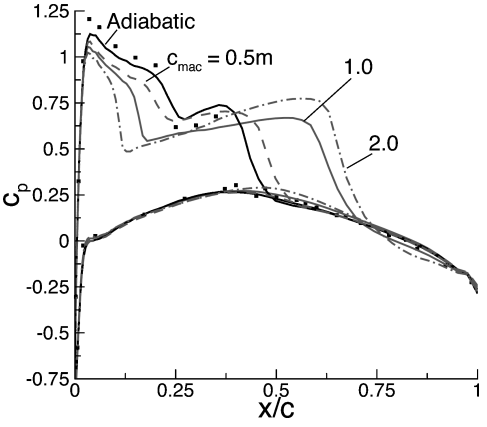


**b) 80% span**

**Fig. 9 ONERA M6 pressure coefficient for different $c_{\text{mac}}$; $M_\infty = 0.84$, $\alpha = 3.06$ deg, $N_{\text{het},0} = 1 \times 10^{12}$ m$^{-3}$, and $R_p = 1 \times 10^{-8}$ m.**

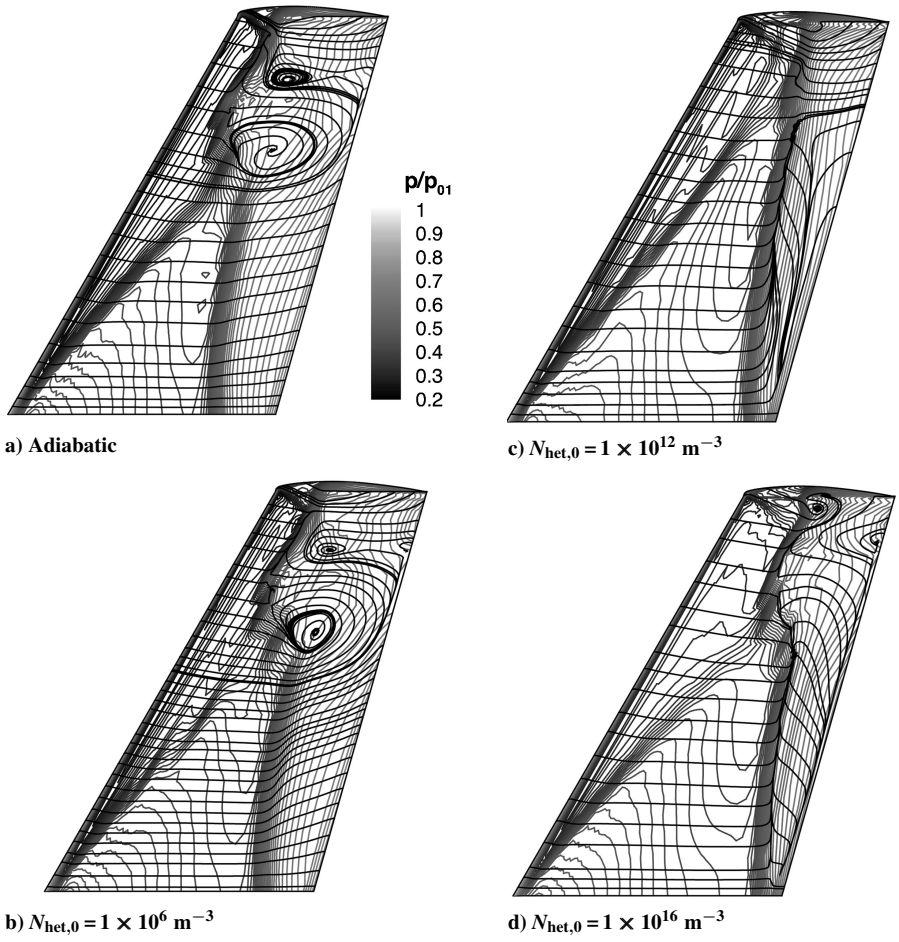


**Fig. 10 ONERA M6 wing top pressure distribution and computed skin friction lines; $M_\infty \approx 0.84$, $\alpha = 6.06$ deg, $c_{mac} = 1.0$ m, and $R_p = 1 \times 10^{-8}$ m.**

distribution and computed skin friction lines for the adiabatic case. Note the large separation region near the tip, which is also present in the experiment. Unfortunately, no oil flow patterns were in the report; thus, the separation zone is inferred from the $c_p$ data. As condensation is increased (Figs. 10b–10d), it has the effect of decreasing the separation region, which decreases drag, but due to the supercritical heat addition at the leading edge, drag is increased, so this balance is observed. The separation region is decreased because the condensation is increasing the static pressure at the leading edge, which lowers the preshock Mach number on this part of the wing. See Fig. 6b, $N_{het,0} = 10^{16}$ m$^{-3}$; there is a new separation zone forming that is due to the shift in shock toward the trailing edge. The preshock Mach number is less than the adiabatic preshock Mach number, but because the shock is occurring on a higher curvature section of the airfoil, separation is occurring.

The change in lift and drag, as well as the lift-to-drag ratio, is used as a final analysis to compare the effects of particle density on $c_{mac}$ length and angle of attack. For all $c_{mac}$ (Fig. 11a), the drag and lift are increasing due to condensation. At $10^{12}$ m$^{-3}$, the largest difference between $c_{mac}$ is present with a trend of a small increase in the ratio as particle density increases. To be numerically honest, Fig. 11b is an expanded scale with a maximum difference between adiabatic and condensing flow of $\approx$4% for $10^{12}$ m$^{-3}$. Thus, care must be taken in determining how much condensation is effecting the flow under these conditions. In Fig. 11b, the drag at $\alpha = 6.06$ deg is relatively constant, with the smallest angle showing the largest increase in drag. The low angle of attack of 1.07 deg shows a constant or slightly decreasing function for the lift-to-drag ratio, whereas for 3.06 and 6.06 deg, there is an increase. Also the contribution of friction is greater for the low angle of attack, accounting for about 10% of the total, compared to 5 and 2.5% for 3.06 and 6.06 deg. Again an expanded scale is used, but with $\alpha = 6.06$ deg, there is a maximum change in the lift-to-drag ratio of about $\approx$10%, where one can argue that there is definitely an effect on wing performance with condensation.

## F-16 Falcon Wing Results

Because the F16 wing airfoil thickness is so small, a freestream Mach number of 0.9 was used as the starting point to achieve a large enough supersonic region, which is needed to see the effect of condensation. For this wing only atmospheric flight conditions will be analyzed ($T_\infty = 293.15$ K and $p_\infty = 1$ bar) because the interest lies in the effect of how lift and drag are affected due to condensation on the real wing geometry of the plane. The parameters for condensation are a particle density of $10^{12}$ m$^{-3}$, particle radius $R_p = 0.01$ $\mu$m, and a freestream humidity of $\phi_\infty = 90$%. Figure 12 shows the pressure coefficient at 38% ($c_{38} = 2.79$ m), and 77% ($c_{77} = 1.81$ m) wing span for the adiabatic and condensing flow case with varying angle of attack. For $\alpha = 0$ and 3 deg, the supersonic region is extended due to heterogenous condensation occurring in this region. Also there is a static pressure decrease after the leading edge for $\alpha = 3$ deg. In addition, near the tip, a double shock system is forming on the wing. At a higher angle of attack, the shock position is unchanged due to condensation being produced only at the leading edge, which is why there is a much larger static pressure increase at the leading edge compared to the earlier two angles. Note that at this high angle of attack there is an absence of heterogeneous condensation; thus, it is pure homogeneous condensation. This effect is similar to what happens in a nozzle with fast expansions, where the timescale of cooling (homogeneous condensation) is small compared to the timescale of the agglomeration of vapor on existing particles.

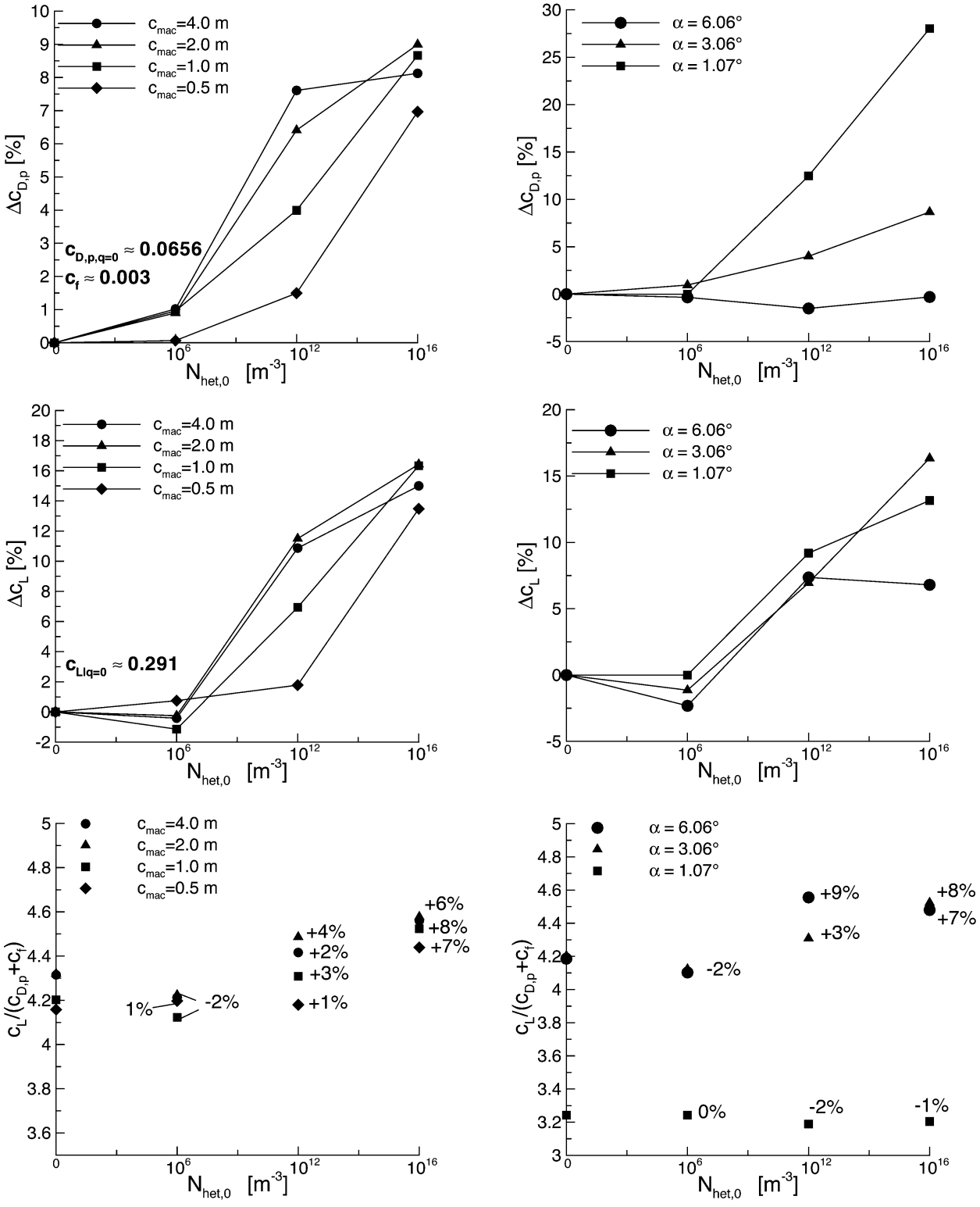


a) $\alpha = 3.06$ deg b) $c_{mac} = 1$ m

**Fig. 11 ONERA M6 wing lift, drag and lift-to-drag ratio as a function of particle density for different $c_{mac}$ and angles of attack; $M_\infty \approx 0.84$ and $R_p = 1 \times 10^{-8}$ m.**

To see the effect of the increase in the supersonic region due to condensation, a Mach contour plot (Fig. 13) of $M > 1$ is shown for the $\alpha = 0$ deg case; the trend is similar for $\alpha = 3$ and 6 deg.

Another case for a freestream Mach number of 1.1 was calculated, but due to space limitations only the final result for the lift-to-drag ratio are shown. Figure 14 shows the effect on the change in lift, drag, and lift-to-drag ratio for the two freestream Mach numbers. In Fig. 14a, due to the high increase in drag at $\alpha = 0$ deg, the ratio decreases compared to the adiabatic case, even for an increase in lift. Only at $\alpha = 3$ deg is there a benefit with condensation. At $\alpha = 6$ deg, the increase in drag is very small, but now there is a decrease in lift because there is no heterogenous condensate to enlarge the supersonic region. For a slightly supersonic freestream (Fig. 14b), the lift-to-drag ratio decreases regardless of the angle of attack, which follows the same trend as the decrease in lift. The main reason for the

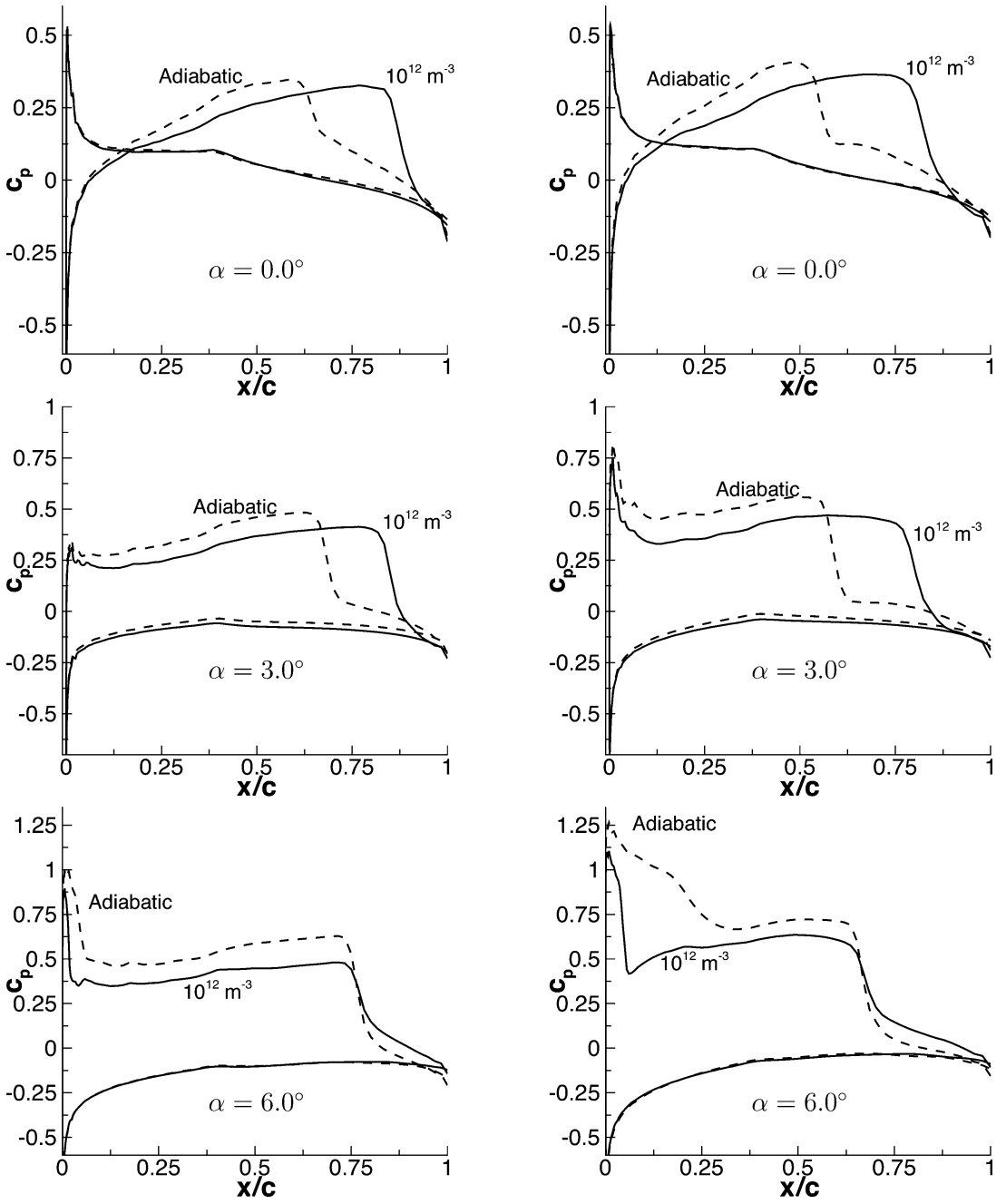


a) 38% span b) 77% span

**Fig. 12 F-16 wing pressure coefficient; $M_\infty = 0.9$, $N_{\text{het},0} = 1 \times 10^{12}$ m$^{-3}$, $R_p = 1 \times 10^{-8}$ m, $c_{\text{mac}} = 2.72$ m, and $Re_{c_{\text{mac}},\infty} = 54.8 \times 10^6$.**

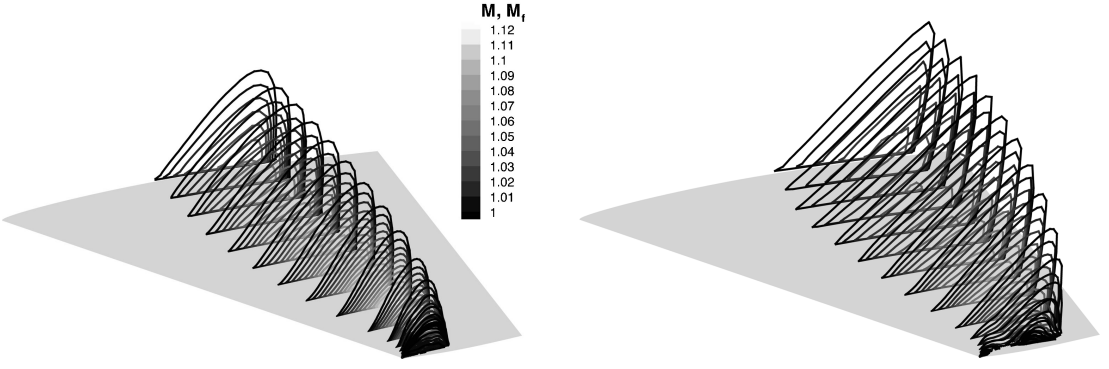


a) Adiabatic b) Condensing flow

**Fig. 13 Supersonic region on upper surface of F-16 wing; $M_\infty = 0.9$, $\alpha = 0$ deg, $N_{\text{het},0} = 1 \times 10^{12}$ m$^{-3}$, and $R_p = 1 \times 10^{-8}$ m.**

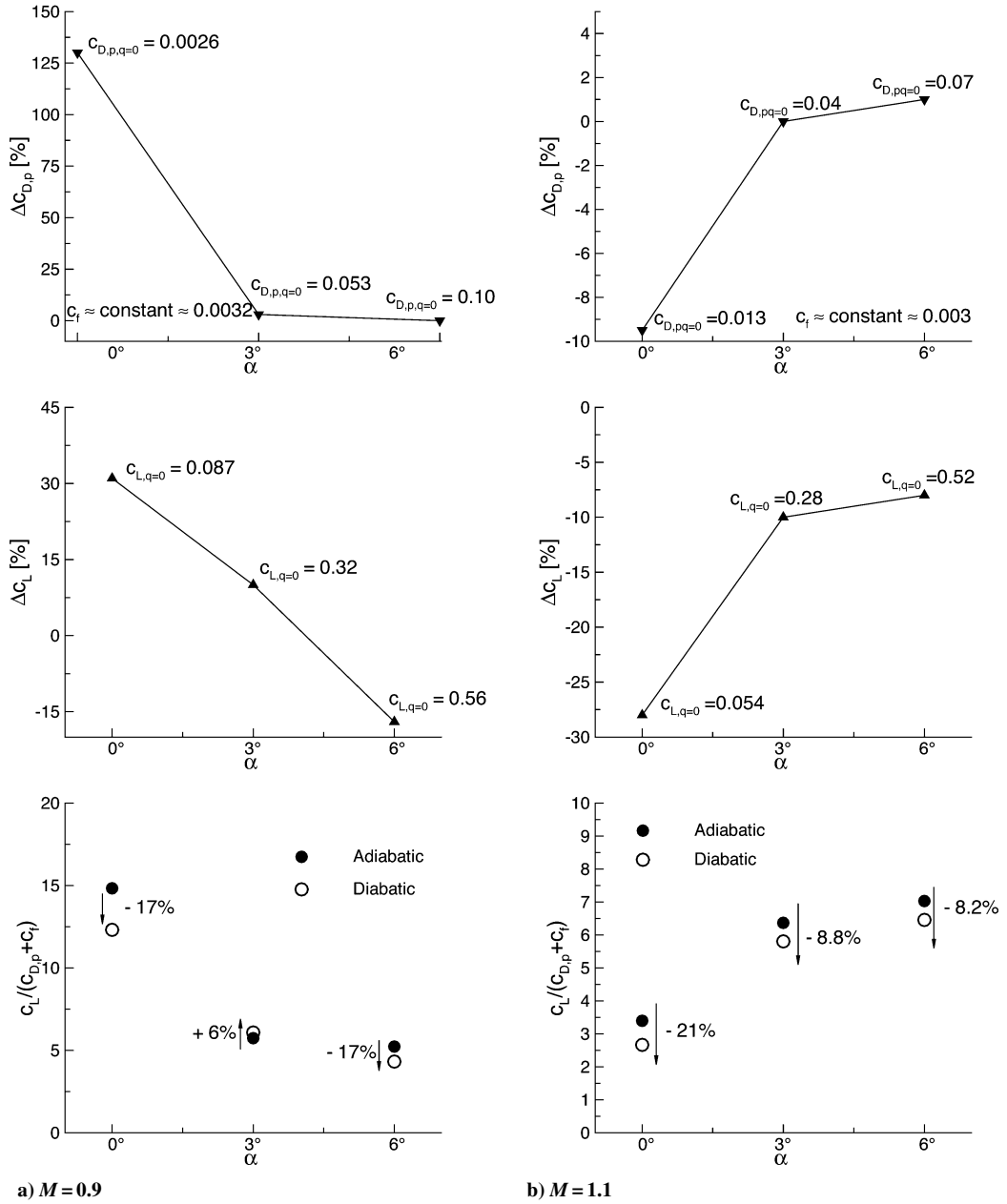


**Fig. 14 F-16 wing lift, drag, and lift-to-drag ratio as a function of angle of attack for different freestream Mach numbers; $N_{het,0} = 1 \times 10^{12}$ m$^{-3}$ and $R_p = 1 \times 10^{-8}$ m.**

**Table 3 Lift-to-drag ratio change due to condensation; $\phi_\infty = 90\%$, $N_{het,0} = 1 \times 10^{12}$ m$^{-3}$, and $R_p = 1 \times 10^{-8}$ m**

| Wing | 0 deg | 1 deg | 3 deg | 6 deg |
|---|---|---|---|---|
| F-16, $M = 0.9$ | −17.0% | | +6.0% | −17.0% |
| F-16, $M = 1.1$ | −21.0% | | −8.8% | −8.2% |
| ONERA M6, 1 m | | −1.6% | +3.0% | +9.0% |
| ONERA M6, 2 m | | | +4.0% | |

decrease in the lift is because heterogeneous condensation can not increase the supersonic region by shifting the shock because the shock occurs at the trailing edge. Table 3 shows change in lift-to-drag ratio of the F-16 and ONERA M6 at different angles of attack.

## Conclusions

There are no current sources that explicitly discuss the change in the lift-to-drag ratio due to heterogeneous condensation. Yamamoto[3] reports a decrease in the lift-to-drag ratio for the ONERA M6 wing for pure homogeneous condensation, which is also found at low particle densities on the ONERA M6 wing. Schnerr and Dohrmann report[2] a decrease in the lift for equilibrium condensation in atmospheric flight on the NACA0012 airfoil at low angles of attack. On the ONERA M6 and F16 wings for the subsonic transonic freestream, the trend is normally an increase in lift due to condensation. This difference is mainly due to the different profiles (shape and maximum thickness), because in the case of the NACA0012, there is a supersonic region on the pressure side that is extended due to condensation that has a negative impact on lift. For the wing conditions, no supersonic region exist on the lower side.

For external atmospheric flight conditions, a wide variety of simulations were performed. In regards to the ONERA M6 wing, the chord, angle of attack, and particle concentration were changed to see their effects. When the mean aerodynamic chord length was increased from 0.5 to 2 m, the effect of heterogeneous condensation was increased. At higher angles of attack of 3 and 6 deg, a mixture of homogeneous and heterogenous condensate is present. For the F-16 wing, only the angle of attack and freestream Mach number were changed to see the effects of condensation at different flight conditions. Table 3 highlights the percent change

in the lift-to-drag ratio of the two wings at different angles of attack.

For supersonic flight, condensation on the F16 wing has a negative impact for any angle, whereas at a subsonic freestream for $\alpha = 3$ deg, there is slight increase in the lift-to-drag ratio. The importance of performing a numerical simulation of condensation is emphasized by the fact that the amount and type of condensation formed is strongly influenced by airfoil shape, airfoil and wing size, angle of attack, freestream conditions, and particle concentration.

Further study could include determining the effect on the lift and drag by relaxing the assumption of constant temperature between droplet and vapor/carrier gas mixture and/or using different droplet growth laws that take into account a larger Knudsen number range (inner Knudsen layer-continuum region). In this study, the heterogeneous modeling is simplified, whereas developing or using modeling techniques that enable a distribution of particle sizes or densities, particle geometries other than spheres, and condensation occurring at a specific location on the particle would contribute to research involving heterogeneous condensation in atmospheric conditions.

## References

[1]Schmitt, V., and Charpin, F., "Presssure Distributions on the ONERA-M6-Wing at Transonic Mach Numbers," Experimental Data Base for Computer Program Assessment, Report of the Fluid Dynamics Panel Working Group 04, AGARD AR 138, May 1979.

[2]Schnerr, G. H., and Dohrmann, U., "Drag and Lift in Nonadiabatic Transonic Flow," *AIAA Journal*, Vol. 32, No. 1, 1994, pp. 101–107.

[3]Yamamoto, S., Hagari, H., and Murayama, M., "Numerical Simulation of Condensation Around the 3-D Wing," *Transactions of the Japan Society for Aeronautical and Space Sciences*, Vol. 42, No. 138, 2000, pp. 182–189.

[4]Yamamoto, S., "Onset of Condensation in Vortical Flow over Sharped-Edge Delta Wing," *AIAA Journal*, Vol. 41, No. 9, 2003.

[5]Benetschik, H., "Berechnung der sub-und Transsonischen Dreidimensionalen Strömung in Verdichtern mit Einem Impliziten Relaxationsverfahren," Fakultät für Maschinenwesen Rheinisch-Westfälischen Technischen Hochschule Aachen, Habilitationsschrift, Germany, 1997.

[6]Rumsey, C. L., and Gatski, T. B., "Recent Turbulence Model Advances Applied to Multielement Airfoil Computations," *Journal of Aircraft*, Vol. 38, No. 5, 2001, pp. 904–910.

[7]Young, J. B., "The Condensation and Evaporation of Liquid Droplets at Arbitrary Knudsen Number in the Presence of an Inert Gas," *International Journal of Heat and Mass Transfer*, Vol. 36, No. 11, 1993, pp. 2941–2956.

[8]Wegener, P. P., and Mack, L. M., "Condensation in Supersonic and Hypersonic Wind Tunnels," *Advances in Applied Mechanics*, edited by H. L. Dryden and T. von Kármán, Academic Press, New York, 1958, p. 423.

[9]Peeters, P., Luijten, C. C. M., and van Dongen, M. E. H., "Transitional Droplet Growth and Diffusion Coefficients," *International Journal of Heat and Mass Transfer*, Vol. 44, 2001, pp. 181–193.

[10]Wada, Y., and Liou, M., "Accurate and Robust Flux Splitting Scheme for Shock and Contact Discontinuities," *SIAM Journal on Scientific Computing*, Vol. 18, No. 3, 1997, pp. 633–657.

[11]Wilcox, D. C., *Turbulence Modeling for CFD*, 2nd ed. DCWIndustries, Inc, La Canada CA, 1998.

[12]Aerospaceweb.org, "Fighter Gallery," The Aircraft Musuem, www.aerospaceweb.org/aircraft/fighter/, 12 Aug. 2003.